

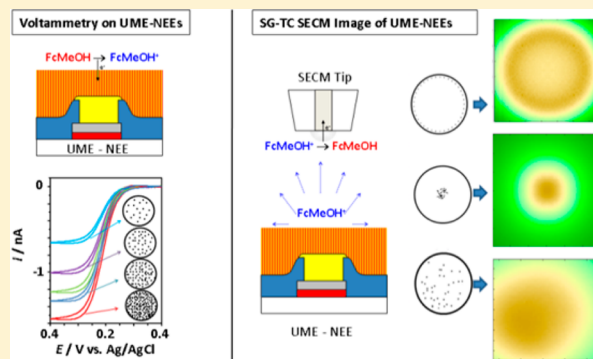
Theory and Experiments for Voltammetric and SECM Investigations and Application to ORR Electrocatalysis at Nanoelectrode Ensembles of Ultramicroelectrode Dimensions

José L. Fernández,[†] Manjula Wijesinghe, and Cynthia G. Zoski*

Department of Chemistry and Biochemistry, New Mexico State University, Las Cruces, New Mexico 88003, United States

S Supporting Information

ABSTRACT: Theoretical and experimental approaches to characterizing nanoelectrode (NE) ensembles of ultramicroelectrode dimensions (UME-NEEs) as a function of fraction of active area and random NE distribution are described. UME-NEEs were fabricated by addressing microregions of a gold-filled polycarbonate membrane through the UMEs of an underlying microfabricated addressable array. Results of Comsol Multiphysics 3D simulations based on randomly spaced NEs of 15 nm radius on a UME disk geometry of radii up to 5 μm are shown for steady-state voltammetry (SSV) and scanning electrochemical microscopy (SECM) experiments. Analytical equations were developed to describe the diffusion-limited steady-state current and steady-state voltammogram at an UME-NEE. These equations are shown to be in good agreement with the simulations and enabled evaluation of experimental SSVs. Comparison of experimental and simulated SECM approach curves, images, and tip voltammograms enabled the fraction of active area and distribution of NEs to be visualized and determined for individual UME-NEEs. Gold UME-NEEs are shown to be unique platforms for electrodeposition in forming nanoparticle electrodes (UME-NPEs). Electrocatalysis results for the oxygen reduction reaction (ORR) on Pt UME-NPEs in 0.1 M H_2SO_4 are also shown.



Ultramicroelectrodes (UME) continue to have a major impact in extending electrochemical methodology into broad new domains of space, time, and chemical media since their development in the late 1970s and early 1980s. This impact is due to well-known attributes of UMES, including high mass transfer rates under steady-state diffusion-limited conditions, a decreased electrical double layer capacitance due to small area, short response times due to a small time constant, and a low ohmic drop. The most popular UME geometry is the disk electrode due to ease of fabrication with a diameter less than 25 μm .^{1–3} The high mass transport rates through enhanced diffusion at UMES are more easily achieved than those by convection at macro-electrodes, which has facilitated the investigation of fast heterogeneous electrode kinetics and mechanisms and the development of methodologies such as scanning electrochemical microscopy (SECM)⁴ and steady-state voltammetry (SSV).^{5–8} The ease in modifying the UME disk geometry has led to the development of networked^{9,10} and tunneling (T-UMES)¹¹ UMES.

We recently reported the development of nanoelectrode ensembles (NEEs) of UME dimensions (UME-NEEs) which are fabricated by securing a Au-filled polycarbonate membrane to a microfabricated addressable array patterned with regularly spaced individually addressable Au UME electrodes each of 10 μm diameter.^{12,13} Microregions of the Au-filled polycarbonate membrane are electrically contacted through the underlying

UMES resulting in a platform of UME-NEEs, which are spaced far enough apart to prevent cross talk between neighboring UME-NEEs. The platform of UME-NEEs is referred to as an addressable NE membrane array (ANEMA).¹³ Each UME-NEE behaves as an UME due to the development of steady-state diffusion layers around individual NEs which may overlap totally, partially, or not at all so that the overall UME geometric area sustains a steady-state flux and current.¹⁴

Metal-filled track-etched polycarbonate membranes were first introduced by Martin as macro-NEEs^{15,16} and have been used in electroanalytical applications^{17,18} and in studies of electron-transfer kinetics.^{18,19} The size and random placement of the disk-shaped NEs of these macro-NEEs are determined by the polycarbonate membrane template and range in sizes of pore radius ($5\text{ nm} \leq R_d \leq 100\text{ nm}$) and porosity ($3 \times 10^8 \leq p \leq 6 \times 10^8\text{ cm}^{-2}$).²⁰ The NEE electroactive area represents a small fraction of the total exposed geometric electrode area which gives rise to current behavior that depends critically on the timescale of the electrochemical experiment, and on the NE radius and spacing so that macro-NEEs largely operate in the transient regime.^{21–27} In contrast, UME-NEEs on the order of 5 μm geometric radius quickly reach a steady state due to the

Received: September 27, 2014

Accepted: December 12, 2014

Published: December 12, 2014



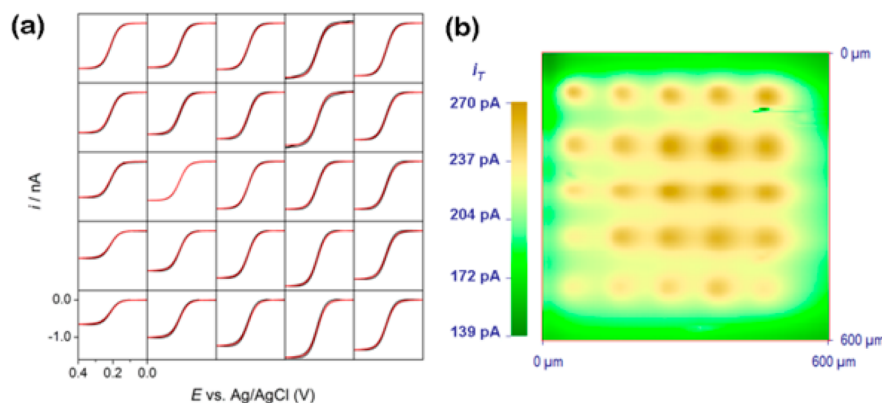


Figure 1. (a) SSVs of individual UME-NEEs of an ANEMA. Scan rate: 5 mV/s. Red lines: theoretical curves from eqs 2–5. (b) SG-TC activity image. Scan rate: 300 $\mu\text{m/s}$. Tip: Pt, $a = 5 \mu\text{m}$ ($\text{RG} \cong 5$), $d = 25 \mu\text{m}$, $E_T = 0 \text{ V}$, $E_S = 0.4 \text{ V}$. Solution: 1 mM FcMeOH/0.1 M KCl. All potentials vs Ag/AgCl.

high mass transport to the individual NEs and to the overall micrometer geometry.^{13,14}

A theory is needed to evaluate the electrochemical activity of UME-NEEs. There is a wealth of literature,^{28–32} including theoretical (e.g., conformal mapping)³⁰ and simulation (e.g., 2D, 3D)^{27–29,31,32} studies describing the fundamental electrochemical behavior of infinite arrays but comparatively fewer for disk arrays of UME dimensions. Phillips considered disk sites on an insulated UME to understand blocking effects by adsorption,³³ Scherson considered disk arrays on a micro-electrode support based on theory adapted from ordered infinite arrays,³⁴ and del Campo showed that the 2D diffusion domain approach for infinite arrays is not appropriate for small square NE arrays due to the importance of the perimeter sites.³⁵ The modeling of UME-NEEs is difficult due to the nonuniform diffusion to individual NEs and to the entire UME geometry.¹⁴

Here SSV and SECM are used in experimentally characterizing individual UME-NEEs in terms of fraction of active area and NE distribution. We report finite element 3D simulations based on randomly spaced NEs of 15 nm radius on a UME disk of radii up to 5 μm . We develop analytical equations to describe the diffusion-limited steady-state current and SSV at a random UME-NEE and use 3D simulations to evaluate these equations. The fraction of active area and random distribution of NEs for individual UME-NEEs were determined through comparison of experimental and simulated SECM approach curves, images, and tip voltammograms. This approach is in contrast to approximate theories based on SECM approach curves to a large, uniformly accessible surface partially covered by randomly distributed nanodisks³⁶ or to charge transfer at partially blocked macro-surfaces of microsites.²³ We also demonstrate the use of SECM tip voltammetry at a UME substrate in contrast to a planar surface as previously reported.^{37–39} Finally, we demonstrate that Au UME-NEEs are novel platforms for Pt electrodeposition in forming nanoparticle electrodes (Pt UME-NPEs) and illustrate their application in electrocatalysis to the oxygen reduction reaction (ORR). NP investigations in electrocatalysis range from NP ensembles (NPEs)^{40–44} to single NP electrodes^{45,46} and single NP collision experiments.^{47–50} Ensemble investigations have largely been carried out on macro-NPEs,⁴³ with more recent work on UMEs as platforms for NPEs.^{51,52} Electrocatalysis at UME-NPEs offer a number of advantages related to the ability to access kinetics under high mass transport, steady-state

diffusion which is difficult to achieve at macro-NPEs. Recent interest in single NP electrodes and NP collision experiments arises from a desire to separate the response on one NP from the ensemble average of a large number of NPs. Thus, investigations on UME-NPEs provide an opportunity to directly investigate NP interaction under high mass transport, steady-state diffusion that is comparable in magnitude to a single NP, thereby bridging the gap between classical ensemble studies on large platforms and isolated single NP investigations.

EXPERIMENTAL SECTION

Chemicals and Materials. All chemicals, listed in the Supporting Information, were of analytical grade and used as received. Nanoporous polycarbonate membranes (PCM, 13 mm diameter, 6 μm thickness) of pore density = $6 \times 10^8 \text{ cm}^{-2}$ and pore diameter = 30 nm; SPI (West Chester, PA).

Instrumentation. Electrochemical experiments were performed using a CHI 660B electrochemical workstation, a CHI 1030 multipotentiostat, and a CHI910B SECM (CH Instruments, Austin, TX). An AR pH meter (Fisher) was used to adjust the pH of electroless plating solutions. Thermal treatments of Au-filled polycarbonate membranes were performed in an Isotemp Model 615G oven (Fisher). An Olympus BX 51 optical microscope (Olympus American Inc., Melville, NY) with an Olympus U-DCIR unit was used to inspect the surface of SECM tips, arrays, and ANEMAs.

Electrodes. SECM Pt tips of 10 μm diameter were fabricated by heat-sealing 10 μm diameter Pt wire in borosilicate glass capillaries under vacuum, followed by polishing and sharpening to a specific RG ($\text{RG} = \text{tip radius}/\text{Pt radius}$).⁵³ Pt tips of 2 μm diameter were fabricated by heat-sealing Pt Wollaston wire after removing the Ag layer by chemical etching in nitric acid.⁵⁴ Ag/AgCl (saturated KCl) and Pt wire (1 mm diameter) were used as reference and counter electrodes, respectively.

Au-Filled Nanoporous Membranes and ANEMAs.

Fabrication of Au nanoporous polycarbonate membranes was performed as reported previously.¹³ ANEMAs were fabricated as previously reported with Au instead of Cu as the electrical contact for the nanoporous membrane.¹³ Both are described in the Supporting Information. Pt was electrodeposited on a group of three UME-NEEs simultaneously by potentiostatic electrodeposition from a 1 mM $\text{H}_2\text{PtCl}_6/0.1 \text{ M H}_2\text{SO}_4$ solution using a CHI 1030 multipotentiostat and Ag/AgCl reference and Pt wire counter electrodes. Electrodeposition potentials

were (A) -0.2 V, (B) -0.3 V, and (C) -0.4 V versus Ag/AgCl, applied for 10 s. The Pt UME-NPEs were observed under an optical microscope; no NPs were detected at a $1000\times$ magnification.

Electrochemical Experiments. CV, LSV, SSV, SECM, and electrocatalysis experiments were performed as described in the Supporting Information.

DIGITAL SIMULATIONS

Comsol Multiphysics 3.5a (COMSOL, Inc., Burlington, MA) with Chemical Engineering Module and Matlab 2011b was used in 3D simulations as described in the Supporting Information.

RESULTS AND DISCUSSION

A typical steady-state voltammogram (SSV) of an ANEMA operating as a single electrode for the oxidation of FcMeOH is shown in Figure S2 of the Supporting Information. Corresponding SSVs of individual UME-NEEs of this ANEMA is shown in Figure 1a. The entire ANEMA defines a SSV with a limiting current that is approximately the sum of the individual diffusion limiting currents of the UME-NEEs, due to the $100\text{ }\mu\text{m}$ center-to-center spacing of each contact UME.

UME-NEE Steady-State Limiting Current. Au NEs of each UME-NEE are randomly spaced at distances which permit total, partial, or no overlap of concentration profiles that grow hemispherically around each single NE.^{13,14} Even though the UME-NEE area is partially covered by an inactive polycarbonate surface, its behavior under total mass-transport conditions will be identical to a disk UME if total overlap of NE concentration profiles occurs. Figure 1a shows some UME-NEEs [e.g., UME-NEEs (1,4) and (1,5); first number refers to the column; the second to the row] that have significantly smaller limiting currents (i.e., $i_L \cong -0.7 - -0.8$ nA) compared to $i_L = -1.5$ nA expected for a $10\text{ }\mu\text{m}$ diameter disk UME. We attribute these changes in the limiting currents to two possible effects. The first is related to the presence of regions on the UME-NEE with poor electrical contact between NEs exposed on the membrane and the underlying Au disk UME. The second is attributed to the presence of a disk edge which is less well-defined than in a disk UME. Together, these effects may lead to a decrease in the effective diameter to a value smaller than the nominal $10\text{ }\mu\text{m}$. However, UME-NEEs can still be used as nanostructured supports as long as their effective radii can be determined from an expression similar to the limiting current due to an oxidation at a disk UME^{55,56}

$$i_{L, \text{UME}} = -4nFDc^b a \quad (1)$$

where a is the radius and other symbols have the usual electrochemical significance.

The limiting current to a UME-NEE can be related to theory describing the flux to an inert sphere covered by randomly placed disk NEs. The theory was developed in the context of trapping species on receptor sites of biological cells.^{57–64} Because a sphere and an inlaid disk behave similarly under diffusion control⁶⁵ and assuming that the support is an inlaid disk of radius a , one can write a diffusion limiting current as

$$i_{L, \text{UME-NEE}} = \frac{-4nFDc^b a f a / R_d \theta}{1 + f a / R_d \theta} = -4nFDc^b a_{\text{eff}} \quad (2)$$

where

$$a_{\text{eff}} = \frac{a^2 f / R_d \theta}{1 + f a / R_d \theta} = \frac{a}{1 + (1 - f) R_d / a f} \quad (3)$$

The effective radius of a UME-NEE is described by a_{eff} where R_d ($R_d \ll a$) is the radius of the NEs which are randomly spaced on the surface. The fraction of the UME-NEE surface which is blocked is designated as θ where $\theta = 1 - N(R_d/a)^2$, and N is the number of NEs corresponding to $p\pi a^2$, where p is the porosity of the membrane (cm^{-2}). The fraction of active area f can be written as $A_{\text{EA}}/A_{\text{GEO}}$ (i.e., the ratio of the electroactive to geometric area), as $(1 - \theta)$, as $p\pi R_d^2$, or as $N(R_d/a)^2$. Thus, the limiting current and effective radius depend on the radius of the supporting UME and of the individual NEs, as well as on the fraction of active (i.e., $f = 1$ corresponds to uniform active area) and blocking (i.e., $f \approx 0$ corresponds to complete blocking) areas. The important parameter for nanostructured microsurfaces such as UME-NEEs is $f a / R_d = p\pi R_d a$ as predicted by Philips.³³ There are two limits for the limiting current and effective radius described by eqs 2 and 3: (a) many NEs, $f a / R_d \gg 1$, so that $a_{\text{eff}} = a$ and i_L is given by eq 1; (b) few NEs, $f a / R_d \ll 1$, so that $a_{\text{eff}} = N R_d$ and $i_L = -4nFDc^b R_d$. Thus, the micrometer dimension of the UME support ensures that a limiting current will be reached in either case.

Figure 2 shows the normalized UME-NEE limiting current (i.e., $i_{L, \text{UME-NEE}}/i_{L, \text{UME}}$) as a function of f for UME support radii

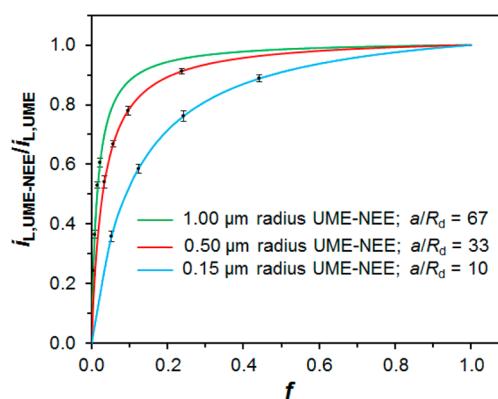


Figure 2. Effect of $f a / R_d$ on UME-NEE normalized limiting current. Simulation parameters: $k^0 = 10\text{ cm/s}$; $E^0 = 0.22\text{ V}$, $\nu = 5\text{ mV/s}$; $C = 1\text{ mM}$; $R_d = 15\text{ nm}$. Error bars represent standard deviation of the average based on three random NE distributions for specific f and radius a . Normalized currents are based on eqs 1–3

0.15, 0.50, and $1.00\text{ }\mu\text{m}$. Solid lines represent normalized currents calculated from eqs 1–3, while solid dots correspond to the average of simulated limiting currents from each of three random NE distributions for a given f on each UME radius (Figure S3 of the Supporting Information). As predicted by eqs 2 and 3, the normalized current rises rapidly to unity as a/R_d increases. For example, $i_{L, \text{UME-NEE}}/i_{L, \text{UME}}$ is within 5% of unity for $a = 0.15\text{ }\mu\text{m}$, $0.50\text{ }\mu\text{m}$, and $1.00\text{ }\mu\text{m}$ when $f = 0.66$, 0.36 , and 0.22 , respectively. Thus, the limiting current for UME-NEEs with a/R_d of 10, 33, and 67 lies within 5% or less of the limiting current for a uniform UME of the respective radius when the coverage of NEs is greater than approximately 70%, 40%, and 20%, respectively.

SSV limiting currents (Figure 1a) of individual UME-NEEs span a range of $0.66\text{ nA} \leq |i_L| \leq 1.56\text{ nA}$, corresponding to an effective UME-NEE radii of $2\text{ }\mu\text{m} \leq a_{\text{eff}} \leq 5\text{ }\mu\text{m}$ and to a

fraction of active area of $0.0023 \leq f \leq 1.0$, calculated from eqs 2 and 3, assuming $a/R_d \approx 333$ and $D = 7.8 \times 10^{-6} \text{ cm}^2 \text{ s}^{-1}$.⁶⁶ The limiting currents and calculated a_{eff} and f are tabulated in Table S1 of the Supporting Information. The approach of experimental $i_{\text{L,UME-NEE}}$ and a_{eff} values as a function of f toward values of -1.5 nA and $5 \mu\text{m}$, respectively, for a disk UME is shown in Figure 3 and Figure S4 of the Supporting

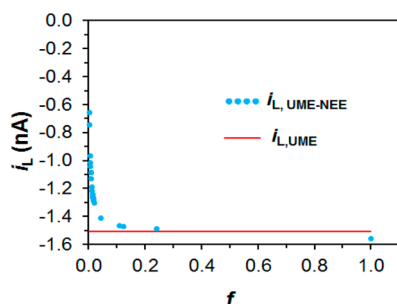


Figure 3. Experimental limiting currents determined from the SSVs of Figure 1a as a function of f . Red line corresponds to the limiting current for a disk UME of a $5 \mu\text{m}$ radius.

Information, respectively. Consistent with simulation results of Figure 2, $i_{\text{L,UME-NEE}}$ and a_{eff} of UME-NEEs based on a $5 \mu\text{m}$ radius UME (i.e., $a/R_d \approx 667$) are within 5% of expected values when $f \geq 0.05$ (i.e., corresponding to $\approx 5\%$ NE coverage).

UME-NEE Steady-State Voltammetry. For the oxidation $R \rightleftharpoons O + e^-$ where Butler–Volmer kinetics are considered, the normalized steady-state current on a UME-NEE is given by

$$\frac{i(E)}{i_{\text{L,UME-NEE}}} = \frac{1}{\frac{1}{\left(\frac{\pi}{4}\right)^{(1-\alpha)F(E-E^0)/RT}} + \gamma e^{-F(E-E^0)/RT} + 1} \quad (4)$$

where

$$\kappa = \left(\frac{k^0 a}{D_R} \right) \left(f + (1-f) \frac{R_d}{a} \right) \quad (5)$$

and $\gamma = D_R/D_O$, where D_i is the diffusion coefficient of R and O, k^0 is the standard heterogeneous rate constant, and α is the symmetry factor. When $f = 1$, $i(E)/i_{\text{L,UME-NEE}}$ corresponds to the normalized steady-state, potential-dependent current at a disk UME. For $f < 1$, the magnitude of the heterogeneous kinetic parameter $k^0 a/D_R$ decreases by the factor relating to the fraction of active and inactive area of the UME-NEE. The normalized steady-state current may appear reversible, quasi-, or irreversible, depending on the contribution of each to the kinetic parameter κ . As $k^0 \rightarrow \infty$, eq 4 reduces to

$$\frac{i(E)}{i_{\text{L,UME-NEE}}} = \frac{1}{1 + (D_R/D_O) e^{-F(E-E^0)/RT}} \quad (6)$$

which describes the reversible steady-state i versus E dependence for a reaction in equilibrium at each potential.^{5–8,65} Figure 4 and Figure S5 of the Supporting Information show the good fit between simulated SSVs at UME-NEE of radii $0.15 \mu\text{m}$, and 1.00 and $0.50 \mu\text{m}$, respectively, for $0.008 < f < 0.5$ with eq 4 and their comparison with a disk UME of corresponding radius, $f = 1$, and reversible kinetics (i.e., $\kappa = \infty$, dashed line). A deviation of 2 mV or less from E^0 at $i/i_L = 0.5$ occurs when $\kappa \geq 15$ and is indistinguishable from the reversible, $f = 1$, SSV.

The red lines in Figure 1a show fittings of eq 4 – 6 to experimental SSVs, which are also shown in Figure S6a of the

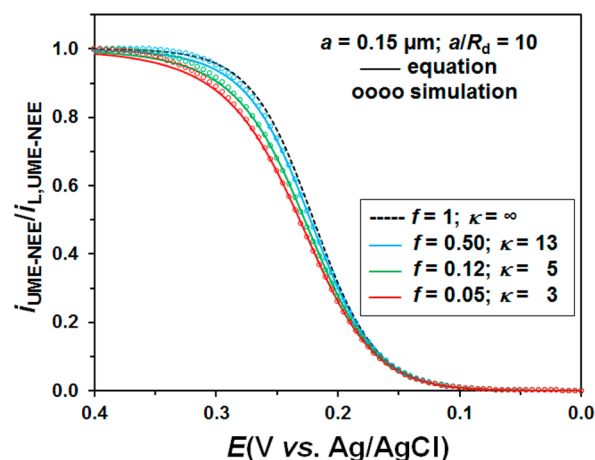


Figure 4. Comparison of SSVs generated from simulations and eq 4–6. $C = 1 \text{ mM}$, $E^0 = 0.22 \text{ V}$, $D = 7.80 \times 10^{-6} \text{ cm}^2/\text{s}$, $\alpha = 0.5$, $k^0 = 10 \text{ cm/s}$.

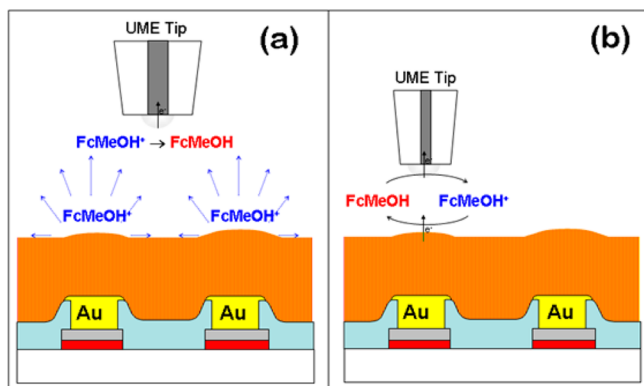
Supporting Information, row-by-row. In all cases, standard potentials determined from the SSVs were almost identical to each other (i.e., $E^0 = 0.210 \text{ V} \pm 0.001 \text{ V}$). Normalized rate constants used in fitting experimental SSVs were far above the limit to distinguish them from the reversible voltammogram ($\kappa > 15$). A good fit of experimental curves with eq 6 for a reversible SSV was found and is expected since the inert spaces of the electrode will have an effect on the limiting current rather than on the electrode reaction kinetics, which are reversible.⁴⁸ This is further demonstrated in Figure S6b of the Supporting Information which shows corresponding normalized SSVs row-by-row. Superimposition of the normalized SSVs is indicative of reversible heterogeneous kinetics.

SECM Imaging. ANEMAs were used as SECM substrates for evaluating the electrochemical activity of individual UME-NEEs. In contrast to SSV where each UME-NEE is individually addressed using a multipotentiostat and multiplexer, individual wiring of each UME-NEE is not necessary in SECM since they are individually addressed by the SECM tip. In the SECM experiments reported here, a single lead was used to connect all 25 UME-NEEs in parallel and to control the potential of the entire ANEMA against a reference electrode. To reach a steady state on the entire ANEMA, the hemispherical concentration profiles that develop around each UME-NEE cannot overlap significantly so that the UME-NEEs behave as independent UMEs. The concentration profiles can be mapped by the SECM substrate generation–tip collection (SG-TC) mode (Scheme 1a) to provide information about electrochemical activity, concentration profile overlapping between adjacent UME-NEEs as well as between adjacent NEs in a UME-NEE, and effective radius.

Figure 1b shows a SG-TC SECM image of FcMeOH^+ concentration profiles corresponding to the individual SSVs of Figures 1a and Figure S6 of the Supporting Information. The concentration of FcMeOH^+ electrogenerated at the NE surfaces was amperometrically sensed by the Pt tip scanned at a constant height. The tip current intensity is a direct measure of FcMeOH^+ concentration and demonstrates that the FcMeOH^+ hemispherical concentration profiles around each UME-NEE are separated well enough to be resolved by the SECM tip.

To understand the SECM images, we discuss considerations important to imaging an UME array in the SG-TC mode. The

Scheme 1. Schematics of (a) SG-TC and (b) Feedback SECM Modes on UME-NEEs of an ANEMA^a



^a(a) SG-TC was used to image FcMeOH oxidation. (b) Feedback was used to perform approach curves and tip voltammetry on individual UME-NEEs.

dependence of the hemispherical concentration profile surrounding an individual UME disk on disk radius a and distance is given by⁶⁷

$$C(r, z) = \frac{2C_s}{\pi} \tan^{-1} \left[\frac{\sqrt{2}a}{\sqrt{(r^2 + z^2 - a^2) + \sqrt{(r^2 + z^2 - a^2)^2 + 4z^2a^2}}} \right] \quad (7)$$

where $C(r, z)$ is the concentration of generated species at radial and axial coordinates r and z measured from the center of the disk, respectively, and C_s is the concentration of generated species at the disk surface. In an array of equally spaced UME disks with identical radii and spaced far enough apart so that no significant overlap occurs, the current of a SECM tip that is scanned at a constant tip–substrate distance should show periodic variations identical from one UME to another, with maximum currents at the centers of the disks. This is observed when imaging a bare array with the UME disks covered with electrodeposited gold (Figure S7 of the Supporting Information). However, if the array disks have different radii, the tip current will vary correspondingly and the maximum tip current will change from one disk to another, as observed in Figure 1b. For example, eq 7 predicts that at a tip–substrate distance of 20 μm , the concentration over the center ($r = 0$) of a disk with $a = 5 \mu\text{m}$ is $C/C_s = 0.156$ while on a disk with $a = 2.5 \mu\text{m}$, $C/C_s = 0.079$, a difference that is proportionally translated to the tip

current. If there were electrical contact problems with the underlying Au disk, a UME-NEE may contain NEs spaced far enough apart that they establish concentration profiles that do not overlap. If this occurs, the concentration of generated species at the center of a 15 nm radius NE at a distance of 20 μm is $C/C_s \cong 0.001$, which cannot be detected by the tip. Thus, tip intensity differences observed in SECM images on different UME-NEEs are most likely related to a decrease in the effective UME-NEE diameter and not to a decrease in f due to electrical contact effects so that the NEs behave independent of each other.

Figure 1b also shows some overlapping of concentration profiles between UME-NEEs where the tip current does not decrease to the background value on the inactive regions. The roughness of the polycarbonate membrane surface (i.e., on the order of ± 100 nm peak-to-valley)¹⁷ may play an important role in this effect, since the magnitude of the overlapping is much smaller on the Au-coated array (Figure S7 of the Supporting Information). Scan rates used in the imaging were relatively high, but there was no improvement in image resolution with slower scanning. Though image resolution was improved by scanning at the same distances using smaller tips (e.g., 1 μm radius), it was never possible to identify concentration profiles from individual NEs. Under conditions of tip–substrate distance and scan rates used in these experiments, the tip ($RG \cong 5$) did not significantly disturb the concentration profiles around the UME-NEEs. Comparison of Figure 1 (panels a and b) demonstrates that both results are in good agreement and are strongly affected by the effective UME-NEE geometric area.

Other factors related to SECM imaging were explored, as described in the Supporting Information. For example, SG-TC imaging experiments were performed on ANEMAs with Au electrodeposits that were considerably overgrown with respect to the silicon nitride surface. Imaging in the tip generation–substrate collection (TG-SC) mode is also described.

SECM Interrogation. An advantage of SECM is the ability to study the electrochemical activity of a well-defined microregion of a substrate by positioning the tip exactly over the region of interest. Using SG-TC imaging based on FcMeOH oxidation at a tip smaller than a typical UME-NEE (e.g., a Pt tip with $a = 1 \mu\text{m}$), a target UME-NEE was selected, and the tip was moved toward its center position by scanning first on a large area and then moving the tip closer and scanning smaller areas at slower scan rates. The resulting SG-TC images are shown in Figure 5.

Simulations were performed to quantify Figure 5b image in terms of NE distribution and f . Simulated images for several

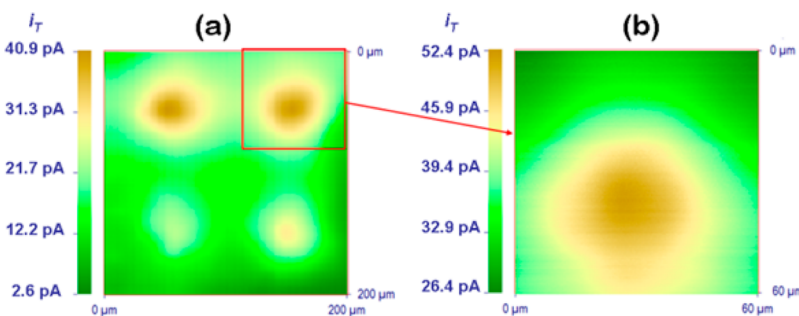


Figure 5. SG-TC activity images of (a) 4 UME-NEEs ($d = 2.2 \mu\text{m}$, $v = 60 \mu\text{m/s}$); (b) 1 UME-NEE ($d = 1.0 \mu\text{m}$, $v = 60 \mu\text{m/s}$) in 1 mM FcMeOH/0.1 M KCl. Tip: Pt, $a = 1 \mu\text{m}$ ($RG \cong 8$), $E_T = 0$ V, $E_S = 0.4$ V vs. Ag/AgCl.

distributions of thirty-seven NEs of 15 nm radius, the best fit in terms of number of NEs, are shown in Figure 6 with the

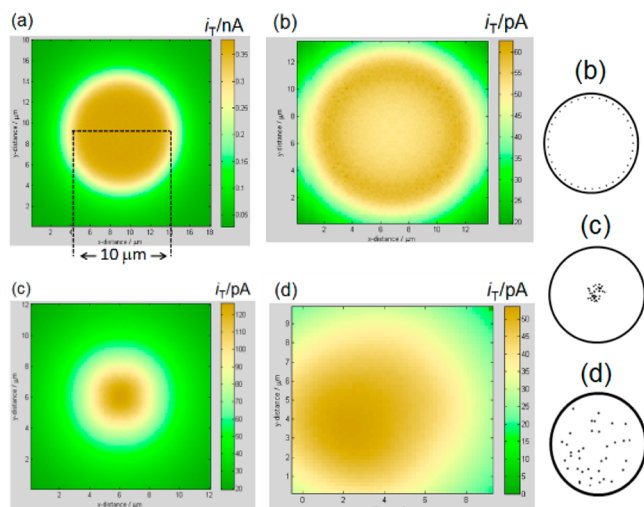


Figure 6. Simulated SECM SG-TC images for random distributions of thirty-seven NEs on UME-NEEs of 5 μm geometric radius. (a) Uniform UME; (b) NEs on the perimeter; (c) NEs in a center circular region of 2 μm diameter; and (d) NEs distributed randomly. Simulation parameters: $k^0 = 10 \text{ cm/s}$; $\alpha = 0.5$; $E^0 = 0.22 \text{ V}$; $c^b = 1 \text{ mM}$; $D = 7.8 \times 10^{-6} \text{ cm}^2 \text{ s}^{-1}$; $d = 1.0 \mu\text{m}$; $a = 1 \mu\text{m}$ ($\text{RG} \cong 8$); $R_d = 15 \text{ nm}$; $f = 0.00033$; $E_T = 0 \text{ V}$; $E_S = 0.4 \text{ V}$ vs Ag/AgCl.

corresponding NE distribution shown to the right of the images. For comparison, Figure 6a shows the simulated image for a 10 μm diameter disk UME where the tip current in the center is $\approx 380 \text{ pA}$. The NEs in Figure 6b are distributed around the perimeter of the UME-NEE leading to a tip image where the current is highest at the perimeter ($\approx 63 \text{ pA}$) and lowest in its center ($\approx 50 \text{ pA}$). The NEs in Figure 6c are distributed in the center of the UME-NEE in a circular region of 2 μm diameter resulting in a tip current which is highest within this circular region ($\approx 127 \text{ pA}$). The simulated image which best matches experimental image Figure 5b is shown in Figure 6d, where the NEs are distributed randomly across the UME-NEE with a maximum current of $\approx 54 \text{ pA}$ in the center.

After positioning the tip over the most active part of the UME-NEE, it was approached at open circuit (OC) to a tip–substrate distance where positive feedback should be detected when polarizing the ANEMA. Steady-state diffusion-limited $i_T/i_{T,\infty}$ versus L approach curves, where $L = d/a$, on partially blocked macro-electrodes have been analyzed by Bard et al. using approximate analytical equations.^{36,68} Here, we use simulations involving an SECM tip in proximity of a UME-NEE substrate and compare these to the experiments.

Figure 7 shows typical approach curves measured on a single UME-NEE; expanded approach curves (Figure S9 of the Supporting Information) confirm that the same limiting tip current is reached at large distances. Similar approach curves were obtained on several other UME-NEEs in the same ANEMA. Experimental approach curves measured under OC conditions were fit with a negative feedback theoretical curve over an insulator. This was also the case for an OC approach to a Au UME, although a slight deviation was detected at the smaller distances (Figure S11 of the Supporting Information). However, approach curves recorded with UME-NEEs at $E_S = 0.0 \text{ V}$ could not be fit with the negative feedback curve over the

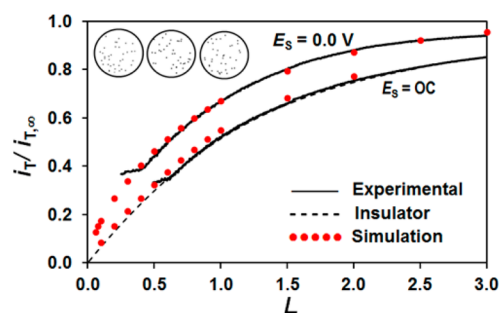


Figure 7. Experimental approach curves for a Pt tip ($a = 1 \mu\text{m}$, $\text{RG} \cong 8$, $E_T = 0.4 \text{ V}$) on a UME-NEE at $E_S = 0.0 \text{ V}$ and at $\text{OC} = 0.09\text{--}1.1 \text{ V}$ (black solid lines). Approach rate: $0.3 \mu\text{m s}^{-1}$. Solution: 1 mM FcMeOH/0.1 M KCl. All potentials vs Ag/AgCl. Solid red dots: simulated points as described in the text. Black dashed line: negative feedback theoretical approach curve over an insulator. Simulation parameters: $k^0 = 10 \text{ cm/s}$; $E^0 = 0.19 \text{ V}$; $c^b = 1 \text{ mM}$; $D = 7.8 \times 10^{-6} \text{ cm}^2 \text{ s}^{-1}$; $a = 1 \mu\text{m}$ ($\text{RG} \cong 8$); $R_d = 15 \text{ nm}$; $f = 0.00033$; $E_T = 0.4 \text{ V}$; $E_S = 0 \text{ V}$ and OC.

whole distance range due to positive feedback from the NEs that regenerated the mediator under diffusion control. A good fit to this approach curve was found with a simulated approach curve generated using the Figure 6d model where thirty-seven NEs of radius $R_d = 15 \text{ nm}$ were distributed randomly on a 5 μm radius circular area. This simulated approach curve (Figure 7) is based on the average response of three random distribution models; individual responses are shown in Figure S10 of the Supporting Information. In comparison, there is significantly greater positive feedback over a Au UME at $E_S = 0.0 \text{ V}$ (Figure S11 of the Supporting Information). The simulated approach curve under OC conditions based on the Figure 6d model is in good agreement with the experimental curve (Figure 7). These results indicate that under OC conditions, the level of positive feedback that is obtained is sensitive not only to the size of the substrate but also to the fraction of connected nanoelectrodes.

SECM tip voltammetry (TV-SECM) was recently described as a method for studies of electrode reactions at large substrates.^{37–39} Here it was used to examine the electrochemical behavior of individual UME-NEEs. In TV-SECM, E_S is held at fixed values over a potential range, including E^0 . The tip responds to concentration profiles generated in the tip–substrate gap as tip potential E_T is ramped linearly. When E_S is held at a value where a uniform substrate and tip perform the same reaction (i.e., $\text{R} \rightleftharpoons \text{O} + ne$, for oxidation), the tip is shielded from the bulk solution by the substrate. For reversible reactions, this means that the tip is exposed to bulk R when $E_S = 0 \text{ V}$ and to substrate-generated O when $E_S = 0.4 \text{ V}$. Tip voltammograms (TVs) (Figure 8b) are composed of an anodic tip current (corresponding to R oxidation) when $E_S = 0 \text{ V}$ and a cathodic tip current (corresponding to substrate-generated O reduction) when $E_S = 0.4 \text{ V}$ as E_T is ramped between negative and positive limits relative to E^0 . The degree of shielding is evident in the cathodic offset of the TV when $E_S = 0.4 \text{ V}$ from that where no shielding occurs (i.e., $E_S = 0 \text{ V}$). Under OC conditions at a finite substrate, E_S is governed by the ratio of the substrate to tip radii and also by the Nernst equation through the local concentrations of FcMeOH and FcMeOH⁺. At $E_T = 0 \text{ V}$, $C(\text{FcMeOH}) \gg C(\text{FcMeOH}^+)$, so that E_S is negative of E^0 . As E_T is scanned positively toward 0.4 V, E_S shifts in order to maintain $i_s = 0$, as the FcMeOH/FcMeOH⁺ concentration ratio changes in the tip–substrate gap due to

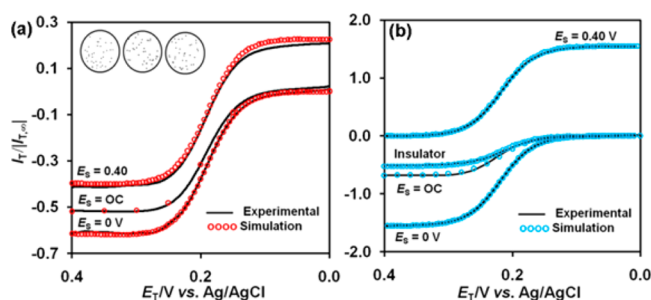


Figure 8. SECM TVs for a Pt tip ($a = 1 \mu\text{m}$, $\text{RG} \cong 8$) positioned over the center of (a) a UME-NEE and (b) a Au UME at $d = 1 \mu\text{m}$, in 1 mM FcMeOH/0.1 M KCl. In (a and b), $E_s = 0.0 \text{ V}$, OC (0.09–0.11 V), 0.4 V. In (b), a TV over a glass surface (i.e., insulator) was recorded. Experimental (solid black lines): scan rate, 50 mV/s; quiet time, 10 s; initial potential, 0 V. All potentials vs Ag/AgCl. Simulation (colored open circles) parameters as in Figure 7, with $\nu = 5 \text{ mV/s}$.

regeneration of FcMeOH as a result of reduction of tip-generated FcMeOH⁺ at the underlying UME-NEE (Figure 8a) or UME (Figure 8b). The magnitude of the FcMeOH/FcMeOH⁺ concentration ratio determines the degree of feedback through i_T and depends on the conductivity (i.e., uniformity) of the underlying substrate.

Figure 8a shows typical experimental and simulated TVs obtained over a single UME-NEE at 0 V, OC, and 0.4 V with a $2 \mu\text{m}$ diameter Pt tip positioned at a tip–substrate distance of $1 \mu\text{m}$ ($L \cong 1$). The simulated TVs are the average response of the three random distributions shown in Figure 7; individual simulations are shown in Figure S12 of the Supporting Information. For $E_s = 0.0 \text{ V}$, the tip is immersed in a solution containing only FcMeOH. As E_T is ramped linearly from 0 to 0.4 V, i_T increases negatively from 0 to a normalized tip current of approximately -0.6 , which is less than the total positive feedback current of approximately -1.5 over a disk UME (Figure 8b). The difference can be attributed to the decrease in FcMeOH feedback due to the small f of the UME-NEE compared to a disk UME. The normalized diffusion controlled i_T is larger in magnitude than that measured from the TV recorded with the UME-NEE at OC. The limiting current at a disk UME at OC ($i_T/i_{T,\infty} \approx -0.68$) was larger in magnitude than that found at the corresponding UME-NEE ($i_T/i_{T,\infty} \approx -0.52$) at OC. Thus, in comparison to the TV recorded over an insulator (Figure 8b), a disk UME at OC gives a detectable positive feedback, while an UME-NEE of the same size responds essentially as an insulator. Limiting tip currents for an UME-NEE held at 0 V and OC are also in agreement with i_T at $d = 1 \mu\text{m}$ from the corresponding approach curves (Figure 7).

For an UME-NEE at $E_s = 0.4 \text{ V}$ for 10 s, a hemispherical diffusion layer of electrogenerated FcMeOH⁺ would extend approximately $90 \mu\text{m}$ into the solution if the UME were uniform. A tip positioned $1 \mu\text{m}$ from the UME surface lies well within this diffusion layer, resulting in a normalized i_T which increases from 0 to 1.5 under total SECM shielding as E_T is ramped linearly (Figure 8b); a cathodic displacement of 1.5 normalized i_T units occurs. In contrast, a TV recorded over an UME-NEE (Figure 8a) shows two limiting current regions (i.e., a normalized anodic current ≈ -0.4 and a normalized cathodic current ≈ 0.2), indicating the tip is exposed to both FcMeOH and FcMeOH⁺. The UME-NEE TV is displaced 0.2 normalized i_T units from the TV recorded for $E_s = 0 \text{ V}$. The shape of the TV does not change, and the difference between the limiting tip currents is 0.6, in agreement with that at $E_s = 0 \text{ V}$. The

subfeedback values for the tip-limiting currents is due to the small f of the UME-NEEs, as confirmed by simulation results.

The good agreement between experiment and simulations for the image, approach curves, and TVs based on the simulation model (Figure 6d) provides a unique method of evaluating the distribution and fraction of NEs on individual UME-NEEs.

Oxygen Reduction on Pt UME-NPEs. By restricting nucleation of electrodeposited Pt to the Au NEs, electrodeposition of single NPs follows the random pattern of the Au-filled membrane. Their size is controlled by judicious selection of electrodeposition time, potential, and waveform. Here, Pt UME-NPEs were fabricated by varying the electrodeposition potential, E_{ed} . The extent of modification was monitored by CV in 0.1 M H₂SO₄ (Figure 9a). For the most positive E_{ed} , CV(A)

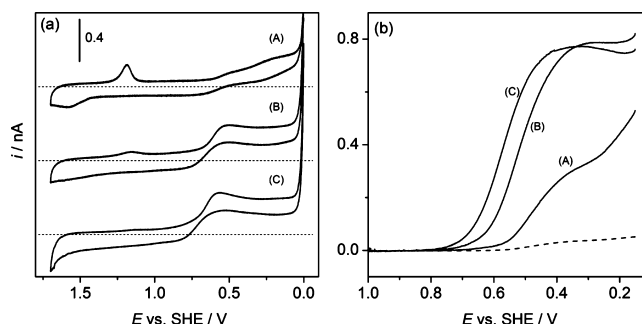


Figure 9. (a) CVs (0.1 V/s) in 0.1 M H₂SO₄ of Pt UME-NPEs fabricated by Pt electrodeposition from 1 mM H₂PtCl₆/0.1 M H₂SO₄ for 10 s at (A) -0.2 V , (B) -0.3 V , and (C) -0.4 V vs Ag/AgCl. Dashed lines: $i = 0$ for each CV. (b) LSVs for the ORR (0.01 V/s) on Pt-UME-NPEs (A), (B), and (C), in 0.1 M H₂SO₄ saturated with O₂ (1 atm). Dashed line: LSV on a Au UME-NEE.

shows typical voltammetric indications of a Au electrode, such as peaks for Au oxide formation and reduction at $E \approx 1.4$ and 1.2 V , respectively. The increase in current at $E < 0.5 \text{ V}$ due to O₂ reduction from dissolved air is an indication of Pt presence. CVs(B) and (C) of Pt UME-NPEs obtained at more negative E_{ed} show a prominent Pt response involving O₂ evolution at $E > 1.5 \text{ V}$, and Pt oxide reduction followed by immediate reduction of dissolved oxygen at $E < 0.7 \text{ V}$. The underpotential deposited (UPD) atomic hydrogen adsorption–desorption peaks commonly observed in polycrystalline Pt electrodes are not clearly defined in these UME-NPEs because the small Pt areas produce adsorption and desorption peak currents that are too small to be distinguished from background currents.⁶⁹ A small peak for Au oxide reduction is still detected at 1.2 V in CV(B), indicating some uncovered Au area, which is almost imperceptible in CV(C).

The electrocatalytic activity for O₂ reduction (ORR: O₂ + 4H⁺ + 4e[−] → 2H₂O) was evaluated in O₂-saturated 0.1 M H₂SO₄ using LSV (Figure 9b). The Au UME-NEE (dashed line) shows very little activity for the ORR, which is only appreciable at $E < 0.5 \text{ V}$, where it reduces O₂ to H₂O₂. The Pt UME-NPE with the smallest amount of Pt [LSV(A)] shows increased activity for O₂ reduction compared to the Au UME-NEE at $E < 0.6 \text{ V}$ and a shoulder at 0.3 V . Assuming that the Pt NPs play a dual catalytic role, LSV(A) suggests that O₂ is reduced to water on the Pt surface and to H₂O₂ on the free Au surface where this latter process is enhanced by the reduction of H₂O₂ by Pt at the Pt–Au interface regions. Increasing the Pt NP size leads to O₂-reduction currents that are significant at

more positive potentials [i.e., $E < 0.75$ V for LSV(B) and $E < 0.8$ V for LSV(C)]. These currents reach a limiting value that is essentially the same on both electrodes and controlled by O_2 diffusion to the UME-NPE. The shift of LSV(C) with respect to LSV(B) can be attributed to the increase in the fraction of Pt area on the apparent rate constant of the O_2 reduction, according to eqs 4 and 5. These experiments are significant in quantifying the effect of the fraction of Pt area on the rate constant of an electrocatalytic reaction under high mass transport conditions.

CONCLUSIONS

We have presented results of experimental and theoretical investigations of UME-NEEs based on random distributions of Au NEs in a polycarbonate membrane. We developed analytical equations for the diffusion-limiting steady-state current and steady-state voltammogram as a function of the fraction of active area, NE size, and effective radius for individual UME-NEEs. The results of these equations are in good agreement with those from 3D simulations.

These equations were used in evaluating experimental SSVs and limiting currents of individual UME-NEEs in order to determine the fraction of active area and effective radius. SSV results were supported by SECM imaging experiments and 3D simulations which provided information regarding the overlapping of concentration profiles around individual NEs. These results indicated that the effective diameter of UME-NEEs is impacted by both the number of NEs around the perimeter in forming a disk edge and the overall fraction of NEs on the effective UME-NEE area. Evaluation of SECM images, approach curves, and TVs was performed through comparison with 3D simulations based on a UME-NEE model of NE distribution. Good agreement was found between experiment and 3D simulations using the same NE distribution model in all cases. Thus, these experiments coupled with corresponding 3D simulations make a powerful method for determining NE distribution and f of UME-NEEs.

Initial investigations on the use of UME-NEEs as templates for Pt NP synthesis showed the potential of these platforms for studying UME-NPEs of varied NP sizes in a preliminary study of the ORR on Pt NP ensembles. The effect of the fraction of Pt-covered area on the polarization curves was qualitatively observed, and interactions between the Pt and Au support, related to hydrogen peroxide reduction, were detected. Further studies for independent visualization of Pt NP size and distribution, and a theory which separates contributions from mass-transport, f , and kinetics, are needed in order to detect possible size effects on the kinetics of the ORR and other reactions of importance in electrocatalysis. Such investigations are underway in this laboratory.

ASSOCIATED CONTENT

Supporting Information

Additional information as noted in the text. This material is available free of charge via the Internet at <http://pubs.acs.org>.

AUTHOR INFORMATION

Corresponding Author

*E-mail: czoski@nmsu.edu. Tel: (575) 646-5292. Fax: (575) 646-2649.

Present Address

†J.L.F.: Facultad de Ingeniería Química, Universidad Nacional del Litoral, Santiago del Estero 2829, (3000) Santa Fe (Santa Fe) Argentina. E-mail: jlferran@fiq.unl.edu.ar.

Notes

The authors declare no competing financial interest.

ACKNOWLEDGMENTS

This work was supported by the National Science Foundation (CHE-0809966, CHE-1408608, C.G.Z.) and a travel grant to J.L.F. by CONICET (Argentina). M. Koudelka-Hep provided the lithographic arrays.

REFERENCES

- (1) Zoski, C. G. *Electroanalysis* **2002**, *14*, 1041–1050.
- (2) Forster, R. J.; Keyes, T. E. In *Handbook of Electrochemistry*; Zoski, C. G., Ed.; Elsevier: Amsterdam, 2007; Ch. 6, pp 155–171.
- (3) Bard, A. J.; Faulkner, L. R. *Electrochemical Methods: Fundamentals and Applications*, 2nd. Ed.; Wiley: N.Y., 2001; Ch. 5, pp 165–176, Ch. 9, pp 360–362.
- (4) *Scanning Electrochemical Microscopy*, 2nd ed.; Bard, A. J., Mirkin, M. V., Eds.; CRC Press, Taylor and Francis: N.Y., 2012.
- (5) Bard, A. J.; Faulkner, L. R. *Electrochemical Methods: Fundamentals and Applications*, 2nd ed.; Wiley: New York, 2001; Chapter 5, pp 180–184, 199–204.
- (6) Zoski, C. G. In *Modern Techniques in Electroanalysis*, Vanysek, P., Ed.; Chemical Analysis Series, Vol. 139, John Wiley and Sons, Inc.: Hoboken, NJ, 1996; pp 241–312.
- (7) Bond, A. M.; Oldham, K. B.; Zoski, C. G. *Anal. Chim. Acta* **1989**, *216*, 177–230.
- (8) Mirkin, M. V.; Bard, A. J. *Anal. Chem.* **1992**, *64*, 2293–2302.
- (9) Dumitrescu, I.; Unwin, P. R.; Wilson, N. R.; Macpherson, J. V. *Anal. Chem.* **2008**, *80*, 3598–3605.
- (10) Adams, K. L.; Jena, B. K.; Percival, S. J.; Zhang, B. *Anal. Chem.* **2011**, *83*, 920–927.
- (11) Kim, J.; Kim, B.-K.; Cho, S. K.; Bard, A. J. *J. Am. Chem. Soc.* **2014**, *136*, 8173–8176.
- (12) Zoski, C. G.; Simjee, N.; Guenat, O.; Koudelka-Hep, M. *Anal. Chem.* **2004**, *76*, 62–72.
- (13) Zoski, C. G.; Yang, N.; He, P.; Berdondini, L.; Koudelka-Hep, M. *Anal. Chem.* **2007**, *79*, 1474–1484.
- (14) Zoski, C. G.; Wijesinghe, M. *Isr. J. Chem.* **2010**, *50*, 347–359.
- (15) Martin, C. R. *Science* **1994**, *266*, 1961–1966.
- (16) Sides, C. R.; Martin, C. R. In *Electrochemistry at the Nanoscale*, Schmuki, P., Virtanen, S., Eds.; Springer: New York, 2009; pp 279–320.
- (17) Ugo, P.; Moretto, L. M. In *Handbook of Electrochemistry*; Zoski, C. G., Ed.; Elsevier: Amsterdam, 2007; Chapter 16, pp 678–709.
- (18) Pozzi Mucelli, S.; Zamuner, M.; Tormen, M.; Stanta, G.; Ugo, P. *Biosens. Bioelectron.* **2008**, *23*, 1900–1903.
- (19) Brunetti, B.; Ugo, P.; Moretto, L. M.; Martin, C. R. *J. Electroanal. Chem.* **2000**, *491*, 166–174.
- (20) Szunerits, S.; Thouin, L. In *Handbook of Electrochemistry*; Zoski, C. G., Ed.; Elsevier: Amsterdam, 2007; Chapter 10, pp 391–428.
- (21) Scharifker, B. R. In *Microelectrodes: Theory and Applications*, Montenegro, M. I., Ed.; Kluwer Academic Publishers: Netherlands, 1991; pp 227–239.
- (22) Amatore, C. In *Physical Electrochemistry: Principles, Methods, and Applications*; Rubinstein, I., Ed.; Marcel Dekker, Inc.: New York, 1995; Chapter 4, pp 131–208.
- (23) Amatore, C.; Saveant, J. M.; Tessier, D. J. *Electroanal. Chem.* **1983**, *147*, 39–51.
- (24) Shoup, D.; Szabo, A. J. *Electroanal. Chem.* **1984**, *160*, 19–26.
- (25) Scharifker, B. R. *J. Electroanal. Chem.* **1988**, *240*, 61–76.
- (26) Szabo, A.; Zwanig, R. J. *Electroanal. Chem.* **1991**, *314*, 307–311.
- (27) Davies, T. J.; Compton, R. G. *J. Electroanal. Chem.* **2005**, *585*, 63–82.

- (28) Guo, J.; Lindner, E. *J. Electroanal. Chem.* **2009**, 629, 180–184.
- (29) Guo, J.; Lindner, E. *Anal. Chem.* **2009**, 81, 130–138.
- (30) Amatore, C.; Oleinick, A. I.; Svir, I. *Anal. Chem.* **2009**, 81, 4397–4405.
- (31) Lee, H. J.; Beriet, C.; Ferrigno, R.; Girault, H. H. *J. Electroanal. Chem.* **2001**, 502, 138–145.
- (32) Beriet, C.; Ferrigno, R.; Girault, H. H. *J. Electroanal. Chem.* **2000**, 486, 56–64.
- (33) Phillips, C. *J. Electrochem. Soc.* **1992**, 139, 2222–2230.
- (34) Zhu, H.; Tolmachev, Y. V.; Scherson, D. A. *J. Phys. Chem. C* **2010**, 114, 13650–13656.
- (35) Godino, N.; Borrisse, X.; Munoz, F. X.; del Campo, F. J.; Compton, R. G. *J. Phys. Chem. C* **2009**, 113, 11119–11125.
- (36) Forouzan, F.; Bard, A. J.; Mirkin, M. V. *Isr. J. Chem.* **1997**, 37, 155–163.
- (37) Zoski, C. G.; Luman, C. R.; Fernandez, J. L.; Bard, A. J. *Anal. Chem.* **2007**, 79, 4957–4966.
- (38) Amemiya, S.; Nioradze, N.; Santhosh, P.; Deible, M. J. *Anal. Chem.* **2011**, 83, 5928–5935.
- (39) Nioradze, N.; Kim, J.; Amemiya, S. *Anal. Chem.* **2011**, 83, 828–835.
- (40) Kwak, J. H.; Kovarik, L.; Szanyi, J. *ACS Catal.* **2013**, 3, 2094–2100.
- (41) Gara, M.; Ward, K. R.; Compton, R. G. *Nanoscale* **2013**, 5, 7304–7311.
- (42) Cong, Y.; Park, H. S.; Wang, S.; Dang, H. X.; Fan, F. R. F.; Mullins, C. B.; Bard, A. J. *J. Phys. Chem. C* **2012**, 116, 14541–14550.
- (43) Zoski, C. G.; Fernandez, J. L.; Imaduwaage, K.; Gunasekara, D.; Vadari, R. *J. Electroanal. Chem.* **2011**, 651, 80–93.
- (44) Lai, S. C. S.; Dudin, P. V.; Macpherson, J. V.; Unwin, P. R. *J. Am. Chem. Soc.* **2011**, 133, 10744–10747.
- (45) Sun, P.; Li, F.; Yang, C.; Sun, T.; Kady, I.; Hunt, B.; Zhuang, J. *J. Phys. Chem. C* **2013**, 117, 6120–6125.
- (46) Li, Y.; Cox, J. T.; Zhang, B. *J. Am. Chem. Soc.* **2010**, 132, 3047–3054.
- (47) Xiao, X.; Bard, A. J. *J. Am. Chem. Soc.* **2007**, 129, 9610–9612.
- (48) Park, J. H.; Boika, A.; Park, H. S.; Lee, H. C.; Bard, A. J. *J. Phys. Chem. C* **2013**, 117, 6651–6657.
- (49) Fernando, A.; Parajuli, S.; Alpuche-Aviles, M. A. *J. Am. Chem. Soc.* **2013**, 135, 10894–10897.
- (50) Zhou, Y.-G.; Rees, N. V.; Pillay, J.; Tshikhudo, R.; Vilakazi, S.; Compton, R. G. *Chem. Commun.* **2012**, 48, 224–226.
- (51) Strmcnik, D.; Hodnik, N.; Hocevar, S. B.; Van der Vliet, D.; Zofko, M.; Stamenkovic, V. R.; Pihlar, B.; Markovic, N. M. *J. Phys. Chem. C* **2010**, 114, 2640–2644.
- (52) Dudin, P. V.; Unwin, P. R.; Macpherson, J. V. *Phys. Chem. Chem. Phys.* **2011**, 13, 17146–17152.
- (53) Fan, F.-R.F.; Fernandez, J.; Liu, B.; Mauzeroll, J.; Zoski, C. G. In *Handbook of Electrochemistry*; Zoski, C. G., Ed.; Elsevier: Amsterdam, 2007; Chapter 6.3.1, pp 189–197.
- (54) Liu, B. In *Handbook of Electrochemistry*; Zoski, C. G., Ed.; Elsevier: Amsterdam, 2007; Chapter 6.3.2, pp 197–199.
- (55) Saito, Y. *Review of Polarography (Japan)* **1968**, 15, 177–187.
- (56) Bond, A. M.; Oldham, K. B.; Zoski, C. G. *J. Electroanal. Chem.* **1988**, 245, 71–104.
- (57) Purcell, E. M. *Am. J. Phys.* **1977**, 45, 3–11.
- (58) Berg, H. C.; Purcell, E. M. *Biophys. J.* **1977**, 20, 193–219.
- (59) Shoup, D.; Szabo, A. *Biophys. J.* **1982**, 40, 33–39.
- (60) Zwanzig, R. *Proc. Natl. Acad. Sci. U.S.A.* **1990**, 87, 5856–5857.
- (61) Zwanzig, R.; Szabo, A. *Biophys. J.* **1991**, 60, 671–678.
- (62) Berezhkovskii, A. M.; Makhnovski, Y. A.; Monine, M. I.; Zitserman, V. Y.; Shvartsman, S. Y. *J. Chem. Phys.* **2004**, 121, 11390–11394.
- (63) Dudko, O. K.; Berezhkovskii, A. M.; Weiss, G. H. *J. Chem. Phys.* **2004**, 121, 1562–1565.
- (64) Makhnovskii, Y. A.; Berezhkovskii, A. M.; Zitserman, V. Y. *J. Chem. Phys.* **2005**, 122, 236102-1–236102-2.
- (65) Oldham, K. B.; Zoski, C. G. *J. Electroanal. Chem.* **1988**, 256, 11–19.
- (66) Miao, W.; Ding, Z.; Bard, A. J. *J. Phys. Chem. B* **2002**, 106, 1392–1398.
- (67) Basame, S. B.; White, H. S. *J. Phys. Chem. B* **1998**, 102, 9812–9819.
- (68) Wei, C.; Bard, A. J.; Mirkin, M. V. *J. Phys. Chem.* **1995**, 99, 16033–16042.
- (69) Tel-Vered, R.; Bard, A. J. *J. Phys. Chem. B* **2006**, 110, 25279–25287.